UCRL--52655

DE83 013647

Distribution Category
UC-35

LAWRENCE LIVERMORE LABORATORY
University of California Livermore, California, 94550

UCRL-52655

SPHERICAL WAVE PROPAGATION IN ELASTIC MEDIA AND ITS APPLICATION TO ENERGY COUPLING FOR TAMPED AND DECOUPLED EXPLOSIONS

Donald B. Larson

MS. date: January 26, 1979

ACKNOWLEDGMENTS

I would like to express my appreciation to P. H. Moulthrop, H. C. Rodean and D. L. Springer for their interest and encouragement in this study, and to M. Heusinkveld and W. J. Hannon for their critical review of the manuscript. I would also like to extend my appreciation to the Department of Energy and the Advanced Research Projects Agency for their financial support.

REFERENCES

1. H. C. Rodean, *Nuclear-Explosion Seismology,* National Technical Information Service, U.S. Dept. of Commerce, Springfield, Va. (1971).
2. J. A. Sharpe, "The Production of Elastic Waves by Explosion Pressures, I. Theory and Empirical Field Observations," *Geophysics 7,* 144-154 (1942).
3. F. G. Blake, Jr., *"Spherical Wave Propagation in Solid Media," J. Acoust. Soc. Am. 24,* 211-214 (1952).
4. A. L. Latter, E. A. Martinelli, and E. Teller, "Seismic Scaling Law for Underground Explosions," *Phys. Fluids 2,* 280-282 (1959).
5. A. L. Latter, R. E. LeLevier, E. A. Martinelli, and W. G. McMillan, "A Method of Concealing Underground Nuclear Explosions," *J. Geophys. Res. 66,* 943-946 (1961).
6. B. F. Murphey, "Particle Motion near Explosions in Halite," *J. Geophys. Res. 66,* 947-958 (1961).
7. D. W. Patterson, "Nuclear Decoupling, Full and Partial," *J. Geophys. Res. 71,* 3427-3436 (1966).
8. J. R. Murphy, "Discussion of the Paper by D. Springer, M. Denny, J. Healy, and W. Mickey, 'The Sterling Experiment: Decoupling of Seismic Waves by a Shot-Generated Cavity,' *J. Geophys. Res. 74,* 6714-6717 (1969).
9. J. R. Murphy, *Seismic Source Functions and Magnitude Determinations for Underground Nuclear Detonations,* ARPA Order No. 1827, Computer Science Corp., Falls Church, Va. (1976).
10. J. R. Murphy and R. A. Mueller, "Seismic Characteristics of Underground Nuclear Detonations Part II: Elastic Energy and Magnitude Determinations," *Bull. Seismo. Soc. Am. 61,* 1693-1704 (1971).
11. R. A. Mueller and J. R. Murphy, "Seismic Characteristics of Underground Nuclear Detonations Part I: Seismic Spectrum Scaling," *Bull. Seismo. Soc. Am. 61,* 1675-1692 (1971).
12. D. B. Larson, *The Relationship of Rock Properties to Explosive Energy Coupling,* Lawrence Livermore Laboratory, Livermore, Ca., UCRL-52204 (1977).
13. W. R. Perret, *"Free-Field Particle Motion from a Nuclear Explosion in Salt. Part I: Project Dribble, Salmon Event,"* Sandia Laboratories, Albuquerque, N.M., VUF-3012 (1966).
14. G. Werth and P. Randolph, "The Salmon Seismic Experiment," *J. Geophys. Res. 71,* 3405-3413 (1966).
15. D. Springer, M. Denny, J. Healy, and W. Mickey, "The Sterling Experiment: Decoupling of Seismic Waves by a Shot-Generated Cavity," *J. Geophys. Res. 73,* 5995-6011 (1968).

SJJ

SPHERICAL WAVE PROPAGATION IN ELASTIC MEDIA AND ITS APPLICATION TO ENERGY COUPLING FOR TAMPED AND DECOUPLED EXPLOSIONS

ABSTRACT

The effects of variation in source and medium properties upon near- and far-field spectra for elastic waves are examined theoretically by considering spherical wave propagation in unbounded elastic media. This type of analysis, although idealized, provides insight into the relative effects of the various source and medium parameters on both tamped and decoupled explosions. It also provides a basis for interpreting both field and laboratory experimental data obtained during spherical wave propagation in real media. In this paper I attempt to unify the work that has been done on spherical wave propagation in elastic media. I present the results in non-dimensional forms, in hopes that others may find these forms of the solutions useful and some of the conclusions, based upon my parameter studies, enlightening. Also included is a discussion of some of the limitations of the theory and examples of applications of the spherical wave propagation theory in real media.

INTRODUCTION

The Department of Energy and the Advanced Research Projects Agency have, for several years, sponsored research related to an understanding of explosion seismology.[1] This research is oriented towards treaty verification and treaty negotiations between the U.S. and the U.S.S.R., but its basic intent is to improve the capabilities for detecting underground explosions and to investigate methods that might be used to conceal such explosions. Since the signing of the Threshold Test Ban Treaty and with the current negotiations directed at a Comprehensive Test Ban Treaty, emphasis has been focused on short-term problems related to these treaties. But the goal, nevertheless, remains the same: develop an understanding of the variability of regional and teleseismic signals produced by underground explosions and, in particular, discover how the explosive yield and the geology surrounding the explosion affect these signals. Another problem to be considered is how seismic signals are produced by earthquakes, and how to distinguish them from signals that might be a result of a suspected treaty violation.

Generally, there are three basic parts to the problem of interpreting seismic signals: (1) the effect of the source region, (2) the effect of the propagation path, and (3) the effect of the receiver region. In this paper only the source region is considered, which I define to include the energy source and enough surrounding geologic material to allow an approach to elastic wave propagation (i.e., out to the "elastic radius" of the geologic medium of interest). This definition is convenient for the objectives of my research because it allows me to determine how the explosive yield and the geological environment surrounding the explosive affect the signals that are produced. There are at least two approaches that can be used to get an understanding of the source region. One approach is to infer the source region description from a large sample of seismic data. Unfortunately, this approach cannot provide a unique description of the source region. A second approach is to attempt to solve the forward problem by developing an approximate mathematical description of the source region based upon experimental information about the source and the geological environment surrounding the source. This latter approach is the one I have chosen to use because it offers not only a challenge but also a chance to get a unique description of the source region.

MATHEMATICAL ANALYSIS

GENERAL PROBLEM

The propagation of divergent, compressional waves in solid media can be examined by mathematical analysis, provided an idealized statement of the problem is used. Consider a spherical cavity or boundary of radius a_0 within a homogeneous, ideally elastic, infinite medium with density ρ, Lamé's constants λ and μ, and compressional wave velocity c to which an arbitrary pressure p(t) is applied at the boundary.

The elastic equation of motion for this problem is:

$$\rho \frac{\partial^2 \vec{\xi}}{\partial t^2} = (\lambda + 2\mu)\, \vec{\nabla}(\vec{\nabla} \cdot \vec{\xi}) - \mu\, \vec{\nabla}(\vec{\nabla} \times \vec{\xi}), \tag{1}$$

where $\vec{\xi}$ is the vector displacement and $\vec{\nabla}$ is the vector differential operator.* The relation

$$\vec{\xi} = \vec{\nabla}\, \psi \tag{2}$$

gives a solution for compressional wave motion, provided the scalar wave equation

$$\frac{\partial^2 \psi}{\partial t^2} = c^2\, \nabla^2 \psi \tag{3}$$

is satisfied where $c^2 = (\lambda + 2\mu)/\rho$.

In spherical coordinates the radial component of Eq. (2) is given by

$$\xi(r,t) = \frac{\partial \psi}{\partial r},$$

and Eq. (3) is

$$\frac{\partial^2 \psi}{\partial t^2} = \frac{c^2}{r^2} \frac{\partial}{\partial r}\left(r^2 \frac{\partial \psi}{\partial r}\right). \tag{4}$$

A reduced displacement potential $\phi(r) = r\, \psi(r,t)$ for outgoing spherical waves can be defined, leading to the equation

$$\frac{\partial^2 \phi}{\partial t^2} = c^2 \frac{\partial^2 \phi}{\partial r^2}$$

with plane wave solutions

$$\phi = \phi_1\left(t + \frac{r}{c}\right) + \phi_2\left(t - \frac{r}{c}\right).$$

In this discussion only the second or outward moving wave will be considered. Using this definition, the displacement is given by

$$\xi(r,t) = \frac{\partial}{\partial r}\left[\frac{\phi(\tau)}{r}\right]$$

*This form of the Navier equation assumes that body forces such as gravity are zero.

or

$$\xi(r,t) = -\frac{1}{rc}\dot{\phi}(\tau) - \frac{\phi(\tau)}{r^2} \tag{5}$$

where $\tau = t - (r - a_0)/c$ is the retarded time (i.e., the time from wave arrival), and $\dot{\phi}(\tau)$ means differentiation with respect to the argument τ.

With an arbitrary pressure* $p(\tau)$ applied at the radius a_0, the boundary condition for this problem is

$$p(\tau) = \left[-(\lambda + 2\mu)\frac{\partial \xi}{\partial r} - 2\lambda\frac{\xi}{r}\right]_{r = a_0} . \tag{6}$$

A solution to this problem in the time domain was given by Sharpe.[2] Under the assumption that $\lambda = \mu$ (i.e., a Poisson's ratio of 1/4) for the driving function $p(t) = p' e^{-\alpha t}$, and where $A = 2\sqrt{2}/3 \cdot c/a_0$, Sharpe found that

$$\phi(\tau) = \frac{a_0 p'}{\rho[(A/\sqrt{2} - \alpha)^2 + A^2]}\left[-e^{-\alpha\tau} + e^{-A\tau\sqrt{2}}\left\{\left(\frac{1}{\sqrt{2}} - \frac{\alpha}{A}\right)\sin A\tau + \cos A\tau\right\}\right], \tag{7}$$

while for a step-function boundary condition $p(t) = p_0$, he found that the potential was given by

$$\phi(\tau) = \frac{2a_0 p_0}{3\rho A^2}\left[-1 + \sqrt{\frac{3}{2}}\, e^{-A\tau\sqrt{3}}\sin(A\tau + \tan^{-1}\sqrt{2})\right]. \tag{8}$$

Without the restriction that $\lambda = \mu$, Blake obtained a slightly more complicated expression for the reduced displacement potential.[3] He found that for the forcing function $p(t) = p' e^{-\alpha t}$

$$\phi(\tau) = \frac{p' a_0}{B^2\rho}\left[-e^{-\alpha\tau} + \frac{B}{F}\, e^{-\alpha_0\tau}\cos(F\tau - E)\right], \tag{9}$$

where $\alpha_0 = (c/a_0)\cdot(1 - 2\sigma)/(1 - \sigma)$, $F = (c/a_0)\cdot(1 - 2\sigma)^{1/2}/(1 - \sigma)$, $B^2 = F^2 + (\alpha_0 - \alpha)^2$, $E = \tan^{-1}(\alpha_0 - \alpha)/F$, and σ is Poisson's ratio.

According to Latter et al., this spherical wave propagation problem can also be solved in the frequency domain.[4] Substitution of Eq. (5) into Eq. (6) gives

$$p(\tau) = \left\{-(\lambda + 2\mu)\frac{\partial}{\partial r}\left[-\frac{1}{rc}\dot{\phi}(\tau) - \frac{\phi(\tau)}{r^2}\right] - \frac{2\lambda}{r}\left[-\frac{1}{rc}\dot{\phi}(\tau) - \frac{\phi(\tau)}{r^2}\right]\right\}_{r = a_0}$$

$$= \left[-\frac{(\lambda + 2\mu)\ddot{\phi}}{rc^2} - \frac{4\mu\dot{\phi}}{r^2 c} - \frac{4\mu\phi}{r^3}\right]_{r = a_0} . \tag{10}$$

The Fourier transform of Eq. (10) gives

$$\bar{p}(\omega) = \left[\frac{\lambda + 2\mu}{rc^2}\,\omega^2\bar{\phi} - \frac{4\mu i\omega}{r^2 c}\,\bar{\phi} - \frac{4\mu}{r^3}\,\bar{\phi}\right]_{r = a_0} .$$

*The pressure (or radial stress) $p(\tau)$ is the boundary condition at the cavity wall or elastic boundary and provides the driving force for the elastic wave propagation. Therefore, by definition, this pressure (or radial-stress) time history contains all effects associated with motion inside the boundary.

where

$$\hat{\phi}(\omega) = \frac{1}{2\pi} \int_0^\infty \phi(\tau)\, e^{i\omega\tau}\, d\tau \quad *$$

and

$$\hat{p}(\omega) = \frac{1}{2\pi} \int_0^\infty p(\tau)\, e^{-i\omega\tau}\, d\tau$$

are the Fourier transforms of $\phi(\tau)$ and $p(\tau)$, respectively, and both $\phi(\tau)$ and $p(\tau)$ are equal to zero for $\tau < 0$. Rearrangement and substitution of $r = a_0$ gives the displacement potential $\hat{\phi}(\omega)$

$$\hat{\phi}(\omega) = \frac{\hat{p}(\omega)a_0^3}{4\mu} \cdot \frac{1}{\beta\eta^2 - i\eta - 1} \quad , \tag{11}$$

where $\beta = (\lambda + 2\mu)\, 4\mu$, $\eta = \omega/\omega_0$, and $\omega_0 = c/a_0$.

Next, the Fourier transform of Eq. (5) is obtained

$$\hat{\xi}(r,\omega) = -\left(\frac{1}{r^2} + \frac{i\omega}{rc}\right)\hat{\phi}(\omega), \tag{12}$$

and Eq. (11) is substituted into (12) to give the desired expression for the displacement as a function of range and frequency

$$\hat{\xi}(r,\omega) = \left(\frac{1}{r^2} + \frac{i\omega}{rc}\right)\frac{\hat{p}(\omega)a_0^3}{4\mu} \cdot \frac{1}{1 + i\eta - \beta\eta^2} \quad . \tag{13}$$

Another useful quantity, the reduced velocity potential $\gamma(\tau)$, can be defined by noting that the particle velocity $u(r,\tau)$ is obtained by taking the time derivative of Eq. (5). Thus,

$$u(r,t) \equiv \frac{\partial \xi(r,t)}{\partial t} = \frac{\partial\left[\frac{\gamma(\tau)}{r}\right]}{\partial r} \quad , \tag{14}$$

where

$$\gamma(\tau) = \dot{\phi}(\tau). \tag{15}$$

The Fourier transforms of Eqs. (14) and (15) give

$$\hat{u}(r,\omega) = i\omega\hat{\xi}(r,\omega) \tag{16}$$

and

$$\hat{\gamma}(\omega) = i\omega\hat{\phi}(\omega). \tag{17}$$

*Notice that in performing a Fourier transform of any function $f(\tau)$, the transformed function $\hat{f}(\omega)$ has the units of $f(\tau)$ multiplied by the units of time.

In the far field (when $r^2 >> rc/\omega$), Eq. (13) reduces to

$$[\tilde{\xi}(r,\omega)]_{ff} = \frac{i\omega\tilde{p}(\omega)a_0^3}{4\mu rc} \cdot \frac{1}{1 + i\eta - \beta\eta^2} \quad . \tag{18}$$

Substitution of Eqs. (11) and (17) into (18) leads to the following simple and useful relationship between the far-field displacements and the reduced-velocity potential

$$[\tilde{\xi}(r,\omega)]_{ff} = -\frac{\tilde{\gamma}(\omega)}{rc} \quad . \tag{19}$$

DECOUPLED FORCING FUNCTIONS

An explosion in a cavity is said to be fully decoupled if the cavity volume is large enough to insure that the surrounding medium responds elastically to the applied pressure p(t). In the practical case, an explosion in the center of the cavity is used to produce the pressure pulse, and the large volume around the explosive allows rapid attenuation of the pressure produced by the explosion. One assumption that has been made is that the pressure pulse closely approximates an ideal step function with the pressure distributed uniformly throughout the cavity.[5] The pressure in this case is given by the expression

$$p_0 = \frac{3\Gamma W}{4\pi a_0^3} \quad , \tag{20}$$

where W is the energy and Γ is a constant characterizing the gas in the cavity.

If we consider a step pressure pulse $p(t) = p_0$ for $t \geq 0$ and $p(t) = 0$ for $t < 0$

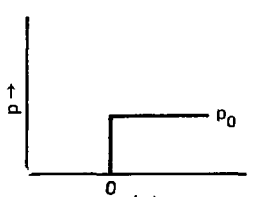

we find that the Fourier transform $\tilde{p}(\omega)$ is given by

$$\tilde{p}(\omega) = \frac{1}{i\omega} \frac{p_0}{2\pi} \quad . \tag{21}$$

Substitution of this result into Eq. (13) gives the displacement $\tilde{\xi}(r,\omega)$

$$\tilde{\xi}(r,\omega) = \left(\frac{1}{r^2} + \frac{i\omega}{rc}\right) \frac{p_0 a_0^3}{i\omega 8\pi\mu} \cdot \frac{1}{1 + i\eta - \beta\eta^2} \quad , \tag{22}$$

which in the far field (when $r^2 >> rc/\omega$) reduces to

$$\tilde{\xi}(r,\omega) = \frac{p_0 a_0^3}{8\pi\mu rc} \cdot \frac{1}{1 + i\eta - \beta\eta^2} \quad . \tag{23}$$

The velocity potential in this case is

$$\tilde{\gamma}(\omega) = -\frac{p_0 a_0^3}{8\pi\mu} \cdot \frac{1}{1 + i\eta - \beta\eta^2} \quad . \tag{24}$$

In Fig. 1 the magnitude of a dimensionless velocity potential $|\tilde{\gamma}^*(\eta)|$ is plotted versus the dimensionless frequency η. (This form is used in presenting the results for convenience in scaling.)

$$|\tilde{\gamma}^*(\eta)| = \frac{|\tilde{\gamma}(\omega)|}{\frac{p_0 a_0^3}{8\pi\mu}} = \left[\frac{1}{1 - (2\beta - 1)\eta^2 + \beta^2\eta^4}\right]^{1/2} \tag{25}$$

Equations (23) and (24) both have the same frequency dependence; therefore, the curves in Fig. 1 also give the frequency dependence of the far-field displacement. The only parameter associated with the medium in Eq. (25) is β, which is related to Poisson's ratio through the elastic constants λ and μ. The maximum value of the magnitude of this dimensionless velocity potential occurs at a dimensionless frequency given by the expression

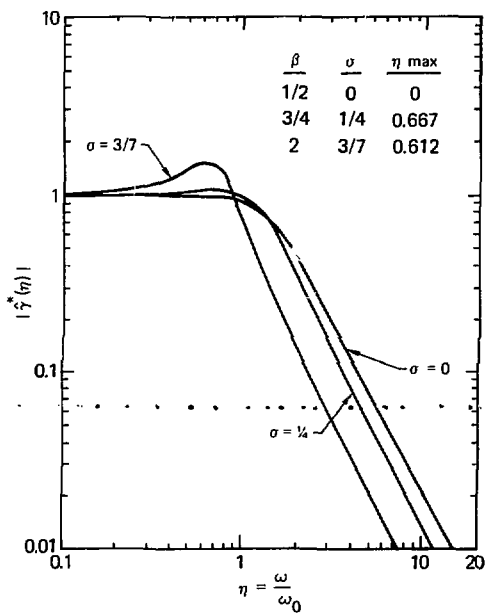

Fig. 1. A dimensionless representation of the reduced velocity potential vs frequency for a step function. The only parameter to be varied is β, which is related to Poisson's ratio through the expression $\sigma = (1 - 2\beta)/(1 - 4\beta)$.

$$\eta_{max} = \sqrt{\frac{2\beta - 1}{2\beta^2}} \quad . \tag{26}$$

In the limit as $\eta \to 0$, the dimensionless velocity potential (Eq. (25)) approaches 1. The dimensionless velocity potential in Fig. 1 remains relatively flat out to frequencies corresponding to $\eta = 0.2$. For stiff materials ($\sigma \lesssim 1/4$), this flat response continues until frequencies near $\eta = 1$. However, very soft materials (i.e., $\sigma \gtrsim 3/7$) show a definite maximum in the potential at frequencies corresponding to the η_{max} of Eq. (26). All materials show a rapid drop in amplitude with frequency beginning near $\eta = 1$, and the slope of the drop approaches -2 at the higher frequencies (as $\eta \to \infty$).*

For the ideal case of a step-pressure function, variations in displacement with frequency in the far field depend only upon the Poisson's ratio of the elastic medium (see Eq. (23)). Therefore, for a given medium, relative amplitudes of displacement at a fixed radius (i.e., decoupling) are determined by ratios of expressions of the form $p_0 a_0^3/8\pi\mu rc$. However, this is only true at low frequencies (when the right-hand side of Eq. (25) is approximately equal to 1). Substitution of Eq. (20) into this expression gives

$$\frac{3\Gamma W}{32\pi^2 \mu r c} \quad . \tag{27}$$

Thus, for a given ideal elastic medium, the displacements in the ideal decoupled medium are proportional to the yield. Equation 27 also shows that decoupling for different media at the same energy W is proportional to the product μc. Therefore, granite ($\mu = 32$ GPa and $c = 6$ km/s) could be approximately three times more effective as a decoupling medium than NaCl ($\mu = 15$ GPa and $c = 4.5$ km/s).† This relation is also true at low frequencies and at all frequencies for different media if c and a_0 can be selected to keep ω_0 equal for the two media.

The actual applied pressure in an explosive-driven, decoupling experiment is a series of narrow, rapidly attenuating spikes resulting from shock wave reverberations in the cavity superimposed on a step-pressure pulse (see, for example, Ref. 6). The first spike is the major perturbation to the step-function assumption, and a measure of its influence (assuming elastic behavior) can be determined by assuming a forcing function of the form

$$p(t) = 0 \text{ for } t < 0$$

$$p(t) = p_1 e^{-\alpha t} + p_0 \text{ for } t \geq 0 \tag{28}$$

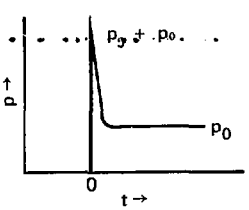

*As a point of interest, note that the vertical separation in this region is related to the ratio of the β's.

†However, the cost of constructing a given cavity in granite would be higher.

where $p_s + p_0$ is the amplitude of the pressure pulse, and α^{-1} is a measure of the width of the pressure spike (i.e., α^{-1} is the time for the spike to decay to an amplitude of $e^{-1}p_s$). The Fourier transform of Eq. (28) is

$$\tilde{p}(\omega) = \frac{1}{2\pi}\left[\frac{p_s}{i\omega + \alpha} + \frac{p_0}{i\omega}\right] \tag{29}$$

so that the non-dimensional magnitude of the reduced velocity potential $|\tilde{\gamma}^*(\eta)|$ becomes

$$|\tilde{\gamma}^*(\eta)| = \frac{|\tilde{\gamma}(\omega)|}{\left(\frac{p_0 a_0^2}{8\pi\mu}\right)} = \left[\frac{\eta^2\left(1 + 2\frac{p_0}{p_s}\right)\left(\frac{p_s}{p_0}\right)^2}{\left(\frac{\alpha}{\omega_0}\right)^2 + \eta^2} + 1\right]^{1/2}\left[\frac{1}{1 - (2\beta - 1)\eta^2 + \beta^2\eta^4}\right]^{1/2} \tag{30}$$

A comparison of the step function (Eq. (25)) with the step function plus pressure spike (Eq. (30)) is given in Fig. 2 using a Poisson's ratio of 1/4. The values of α (5000 s^{-1}) and p_s/p_0 (19.63) were selected based on cavity pressure measurements made on the Cowboy Experiments[6] and on calculations made by Patterson.[7]

Another useful way of examining the effect of a single spike as compared to a step-function input is to take the ratio of Eqs. (30) and (25). This gives relative effects as a function of the dimensionless frequency η.

$$\mathcal{R} = \left[\frac{\eta^2\left(1 + 2\frac{p_0}{p_s}\right)\left(\frac{p_s}{p_0}\right)^2}{\left(\frac{\alpha}{\omega_0}\right)^2 + \eta^2} + 1\right]^{1/2} \tag{31}$$

Figure 2 clearly shows the large effect that a single spike can have upon the higher frequency part of the spectrum considered in Fig. 2. The spike causes a substantial shift in frequency of maximum amplitude (i.e., η_{max})

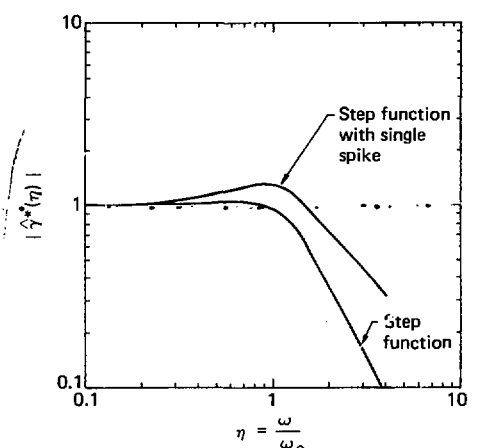

Fig. 2. A non-dimensional plot of Eqs. (25) and (30) using a Poisson's ratio of 1/4.

and decreases the slope of the dropoff as compared to a step function without a spike for frequencies corresponding to several times η_{max}. However, in the limit as $\eta \to \infty$, both of these curves will approach a slope of -2 and will be separated by a factor $p_c/p_0 + 1$.

TAMPED FORCING FUNCTIONS

A tamped explosion is one in which the medium is initially packed around the explosive. The explosion produces a complex sequence of events in the medium, including propagation of a shock wave and growth of a cavity. The shock wave causes inelastic deformation of the surrounding medium until the stress decays to a level of elastic response. The radius at which elastic response begins is called the elastic radius or the boundary for elastic response. The stress–time history that occurs at this radius is the forcing function $p(r)$ in Eq. (6).

Cavity growth is the result of the extremely high pressures released by the explosion, compressing the rock both inelastically and elastically. This causes radial particle motion and displacements to occur as the shock wave passes. Gas pressure within the cavity will continue to drive the cavity expansion at late times until an equilibrium of forces is established.

Generally, the overall result of these processes is a peak in displacement which is reached as the shock wave passes, and then a relaxation to a permanent displacement.* In consolidated (very low porosity) rock, the permanent displacement should be consistent with the incompressible expansion around the cavity or elastic boundary. The permanent displacement, ξ_p, in this case is given by

$$\xi_p = r_f - r \quad ,$$

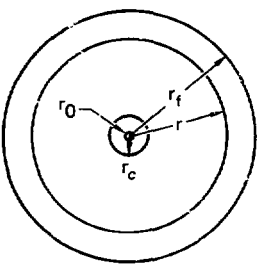

where $r_c^3 - r_0^3 = r_f^3 - r^3$, and where r_0 is the original radius of the explosive, r_c is the radius of the cavity, r is the original position of a mass point in the elastic region, and r_f is the final position of that mass point. In this case,

$$r_f = [r^3 + r_c^3 - r_0^3]^{1/3} \quad ,$$

which gives

$$\xi_p = \left(r^3 + r_c^3 - r_0^3\right)^{1/3} - r \quad .$$

*Much later, as the gases cool and condense, the pressure is relieved causing an imbalance of forces and partial, or in the case of a highly fractured material complete, collapse of the cavity may occur.

For $r >> r_c >> r_0$, the permanent displacement is approximately

$$\xi_p(r) \cong \frac{1}{3}\frac{r_c^3}{r^2} \quad . \tag{32}$$

In cases where porosity is significant, the permanent displacement in the elastic regime will be significantly less than that given by Eq. (32) and dependent upon the amount of volume lost in the crushing of pores.

In an ideal elastic material the permanent displacement can be showa to be related to $\phi(\infty)$ by letting $\tau \to \infty$ in Eq. (5) and assuming that $\phi(\tau)$ approaches a constant value as $\tau \to \infty$. This gives

$$|\xi_p(r,\infty)| = \frac{|\phi(\infty)|}{r^2} \quad . \tag{33}$$

The value $|\phi(\infty)|$ can be determined from Eq. (10) by letting $\tau \to \infty$ and assuming that $\phi(\tau)$ approaches a constant value as $\tau \to \infty$. This gives

$$|\phi(\infty)| = \frac{p_1 a_0^3}{4\mu} \quad , \tag{34}$$

where p_1 is the steady-state final pressure. Substitution of Eq. (34) into Eq. (33) gives

$$|\xi_p(r,\infty)| = \frac{p_1 a_0^3}{4\mu r^2} \quad . \tag{35}$$

Thus, the permanent displacement in the elastic region at a radius r is related to the steady state pressure at the cavity or boundary wall, p_0, as indicated in Eq. (35).

The forcing function chosen by Sharp[2] and Blake[3] to simulate a tamped explosion was

$$\begin{aligned} p(t) &= 0 \text{ for } t < 0 \\ p(t) &= p' e^{-\alpha t} \text{ for } t \geq 0 \end{aligned} \tag{36}$$

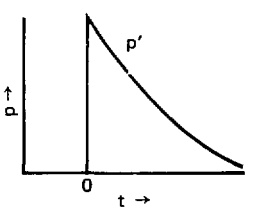

For this function $|\phi(\infty)|$ is zero, and there is no permanent displacement [see Eq. (7)].

The Fourier transform of p(t) is

$$\tilde{p}(\omega) = \frac{p'}{2\pi(\alpha + i\omega)} \quad . \tag{37}$$

Substitution into Eq. (13) gives

$$\tilde{\xi}(r,\omega) = \left(\frac{1}{r^2} + \frac{i\omega}{rc}\right) \frac{p' a_0^3}{8\pi\mu(\alpha + i\omega)} \cdot \frac{1}{1 + i\eta - \beta\eta^2} \quad , \tag{38}$$

and in the far field

$$\tilde{\xi}(r,\omega) = \frac{p' a_0^3}{8\pi\mu rc} \cdot \frac{i\eta}{\left(\frac{\alpha}{\omega_0}\right) + i\eta} \cdot \frac{1}{1 + i\eta - \beta\eta^2} \quad . \tag{39}$$

The reduced velocity potential is given by

$$\tilde{\gamma}(\omega) = -\frac{p' a_0^3}{8\pi\mu} \cdot \frac{i\eta}{\left(\frac{\alpha}{\omega_0}\right) + i\eta} \cdot \frac{1}{1 + i\eta - \beta\eta^2} \quad . \tag{40}$$

In Fig. 3 the dimensionless velocity potential $|\tilde{\gamma}^*(\eta)|$ is plotted for various values of (α/ω_0) with $\beta = 1$ (for a Poisson's ratio of 1/3) where $|\tilde{\gamma}^*(\eta)|$ is given by

$$|\tilde{\gamma}^*(\eta)| = \frac{|\tilde{\gamma}(\omega)|}{\left(\frac{p' a_0^3}{8\pi\mu}\right)} = \eta \left[\frac{1}{\left(\frac{\alpha}{\omega_0}\right)^2 + \eta^2}\right]^{1/2} \left[\frac{1}{1 - (2\beta - 1)\eta^2 + \beta^2\eta^4}\right]^{1/2} \quad . \tag{41}$$

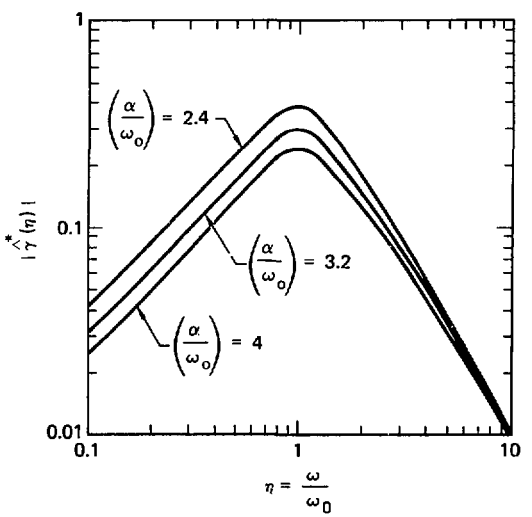

Fig. 3. A dimensionless representation of Eq. (41) for $\beta = 1$ and for various values of the ratio (α/ω_0).

Values of η corresponding to the maximum velocity potential are given by

$$\left(\frac{\alpha}{\omega_0}\right)^2 + \left[(2\beta - 1) - \beta^2\left(\frac{\alpha}{\omega_0}\right)^2\right]\eta^4 - 2\beta^2\eta^6 = 0 \quad , \tag{42}$$

which was obtained by taking the derivative of Eq. (41) and setting it equal to zero. Some solutions of Eq. (41), accurate to the nearest hundredth, are given below to demonstrate the variation of corner frequency, η_{max}, with β and $(\alpha/\omega_0)^2$:

	η_{max}	$(\alpha/\omega_0)^2$
$\beta = 1$	0.89	1
	0.98	10
	0.99	20
$\beta = 2$	0.68	1
	0.70	10
	0.70	20
$\beta = 3.4$	0.97	1
	1.12	10
	1.13	20

The dimensionless velocity potential for Eq. (41) approaches 0 as $\eta \to 0$. The slopes of the curves in Fig. 3 approach 1 and have a separation proportional to ω_0/α as $\eta \to 0$. The slope as $\eta \to \infty$ is -2.

A second forcing function representation for tamped explosions is that given by Eq. (28).

$$\begin{aligned} p(t) &= 0 \text{ for } t < 0 \\ p(t) &= p_s e^{-\alpha t} + p_0 \text{ for } t \geq 0 \end{aligned} \tag{28}$$

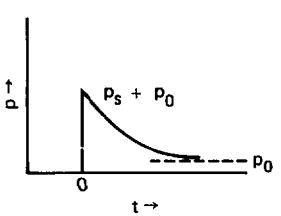

This form has been used extensively by Murphy,[8,9,10] and Mueller[11].

The Fourier transform of Eq. (28) is given by Eq. (29)

$$\bar{p}(\omega) = \frac{1}{2\pi}\left[\frac{p_s}{i\omega + \alpha} + \frac{p_0}{i\omega}\right] \quad , \tag{29}$$

and the dimensionless velocity potential $|\bar{\gamma}^*(\eta)|$ is given by Eq. (30)

$$|\bar{\gamma}^*(\eta)| = \frac{|\bar{\gamma}(\omega)|}{\frac{p_0 a_0^3}{8\pi\mu}} = \left[\frac{\eta^2\left(\frac{p_1}{p_0}\right)^2\left(1 + 2\frac{p_0}{p_s}\right)}{\eta^2 + \left(\frac{\alpha}{\omega_0}\right)^2} + 1\right]^{1/2}\left[\frac{1}{1 - (2\beta - 1)\eta^2 + \beta^2\eta^4}\right]^{1/2} . \tag{30}$$

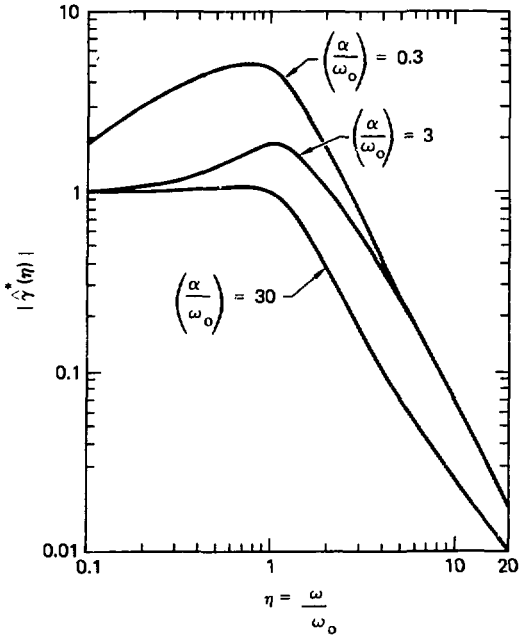

Fig. 4. A dimensionless representation of Eq. (30) with $\beta = 3/4$, $p_0/p_s = 0.238$, and (α/ω_0) allowed to vary.

In Fig. 4, Eq. (30) is plotted with $(p_0/p_s) = 0.238$, $\beta = 3/4$ and (α/ω_0) allowed to vary from 0.3 to 30. In Fig. 5, the effect of varying (p_0/p_s) between 0.1 and 1 is examined with $\beta = 3/4$ and $(\alpha/\omega_0) = 3.0$.

In Fig. 4, for a fixed ratio of (p_0/p_s), we see the effect that the ratio of the characteristic time ω_0^{-1}, associated with the elastic radius a_0 (i.e., $\omega_0^{-1} = a_0/c$) to the measure of the width of the pressure pulse α^{-1}, has upon the spectrum. Thus, for large ratios, $\alpha/\omega_0 = 30$, the spectrum is similar to that for a step function up to frequencies corresponding to $\eta = 1$, but for frequencies beyond that point there is an increasing amount of high-frequency content. For small ratios of (α/ω_0) $(\alpha/\omega_0 = 0.3)$, the pressure pulse is broad and contributes greatly to the amplitude of the potential at all frequencies. However, for very high frequencies (e.g., $\eta \simeq 100$) all three curves converge.

In Fig. 5, with (α/ω_0) and β held constant, we see the effect of varying the ratio of the steady-state pressure p_0 to the spike pressure p_s. As the ratio is made smaller the influence of the spike increases, and large increases in amplitude are seen for all frequencies beyond $\eta \simeq 0.2$. As the ratio is made larger the influence of the spike diminishes and the spectrum begins to approach that expected for a step function. (In the limit as $p_s \to 0$, Eq. (30) gives the step-function solution.)

To determine the effect that a finite rise time has upon the far-field spectra, a forcing function of the form

$$p(t) = 0 \text{ for } t < 0$$
$$p(t) = p_0(1 - e^{-\alpha t}) \text{ for } t \geq 0 \qquad (43)$$

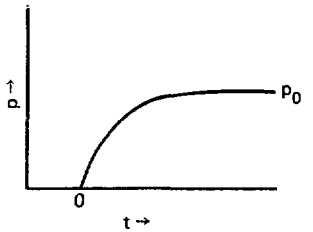

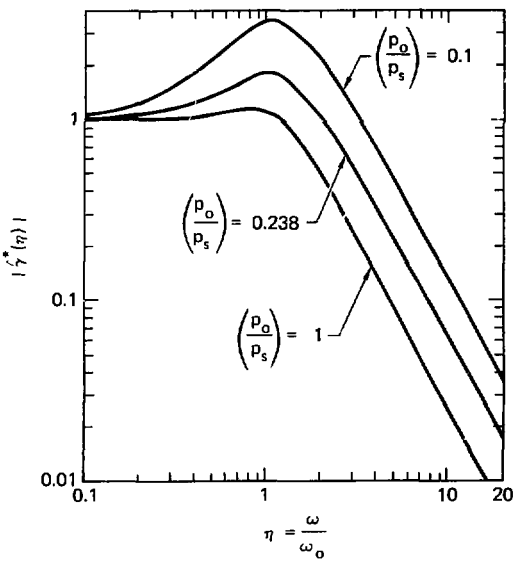

Fig. 5. A dimensionless representation of Eq. (30) with $\beta = 3/4$, $(\alpha/\omega_0) = 3$, and (p_0/p_s) allowed to vary.

was chosen. The Fourier transform in this case is

$$\tilde{p}(\omega) = \frac{p_0}{2\pi}\left(\frac{1}{i\omega} - \frac{1}{i\omega + \alpha}\right) \quad . \tag{44}$$

Substitution of Eq. (44) into Eq. (13) gives for the displacement

$$\tilde{\xi}(r,\omega) = \left(\frac{1}{r^2} + \frac{i\omega}{rc}\right)\left(\frac{p_0 a_0^3}{8\pi\mu}\right)\left(\frac{1}{i\omega} - \frac{1}{i\omega + \alpha}\right)\left(\frac{1}{1 + i\eta - \beta\eta^2}\right) \quad . \tag{45}$$

The corresponding velocity potential is

$$\tilde{\gamma}(\omega) = \frac{p_0 a_0^3}{8\pi\mu}\left(\frac{\frac{\alpha}{\omega_0}}{i\eta + \frac{\alpha}{\omega_0}}\right)\left(\frac{1}{1 + i\eta - \beta\eta^2}\right) \quad . \tag{46}$$

The dimensionless velocity potential $|\tilde{\gamma}^*(\eta)|$ is given below and plotted in Fig. 6 to show the effect of variations in the ratio (α/ω_0) for the case where $\beta = 3/4$.

$$|\tilde{\gamma}^*(\eta)| = \frac{|\tilde{\gamma}(\omega)|}{\left(\frac{p_0 a_0^3}{8\pi\mu}\right)} = \left[\frac{\left(\frac{\alpha}{\omega_0}\right)^2}{\eta^2 + \left(\frac{\alpha}{\omega_0}\right)^2}\right]^{1/2}\left[\frac{1}{1 - (2\beta - 1)\eta^2 + \beta^2\eta^4}\right]^{1/2} \quad . \tag{47}$$

Figure 6 shows that where $\alpha = \omega_0$, all frequencies about $\eta \simeq 0.6$ are strongly attenuated with attenuation increasing with frequency. However, when $\alpha^{-1} = (1/10)\omega_0^{-1}$, the attenuation is very small except at frequencies beyond $\eta \simeq 4$. As $\eta \to 0$ in Eq. (47), the dimensionless velocity potential approaches 1, and as $\eta \to \infty$, the slopes of the curves in Fig. 6 approach −3. (Based upon laboratory and field measurements, these two extremes in rise time probably closely represent the effects to be expected from a dry, weak, highly porous material such as alluvium, and from salt or other materials having little or no dry porosity.[12, 13] The slow rising wave in the dry, weak, highly porous material is a result of dispersion as the pores are crushed by the shock wave.)

THEORY LIMITATIONS

The application of this simple theory to problems associated with real materials has limitations. Thus far in this paper we have merely examined exact solutions based upon the ideal conditions assumed in our mathematical description. To apply these results to real materials requires several assumptions. Before drawing any conclusions based upon application of this theory to real materials, we must be cognizant of the assumptions that are made and understand the sensitivity of the results to the assumptions.

The first assumption is that we are dealing with elastic materials. This is not strictly true for geologic media. There remains significant attenuation of the wave even though most geologic materials appear to approach elastic behavior beyond a certain radius in spherical divergent flow. Typically, this attenuation is atttributed to internal friction, Q^{-1}, and is often described in terms of an exponential attenuation function

$$A(r,\omega,Q^{-1}) = A_0 e^{-\omega r 2Q} \quad . \tag{48}$$

Assuming this type of attenuation law holds beyond the elastic radius, a_0, the higher frequencies will be much more strongly attenuated than the lower frequencies, and attenuation will increase with both radius and internal friction (Fig. 7). In principal, corrections to the simple theory resulting from this inelastic response can be made provided values of Q^{-1} are available. An example of this type of correction is discussed in the next section.

A second assumption is that an elastic radius can be defined. In a decoupled cavity, the cavity radius is the elastic radius; therefore, selection of the elastic radius for cavity shots depends on whether the cavity was or was not overdriven. The elastic radius for tamped explosions is more difficult to define. In real materials, elastic behavior is only approached; therefore, a finite elastic radius can only be defined if we assume that it is the radius beyond which no major inelastic deformation exists. In most solids, shock wave-induced yielding occurs at some finite stress, and below this stress the wave velocity is approximately equal to the sound speed. Therefore, it seems logical to define the elastic radius in a medium as the radius beyond which the stress is less than, or equal to, the dynamic yield stress. The major problem, however, is to determine a representative value of this stress for the geologic media of interest.

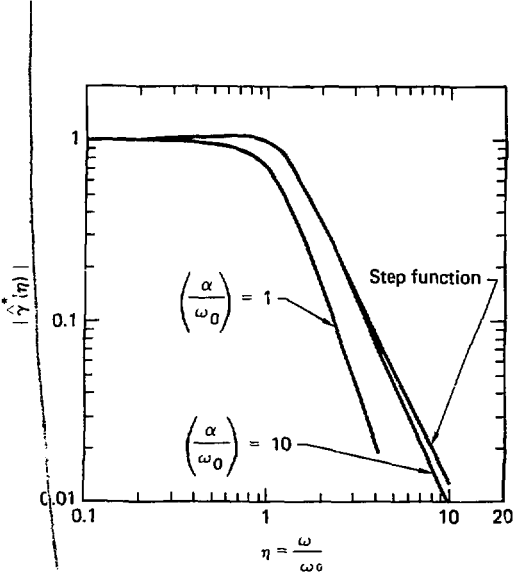

Fig. 6. A dimensionless representation of Eq. (47) with $\beta = 3/4$, showing the effect that the rise time α^{-1} has upon the spectrum.

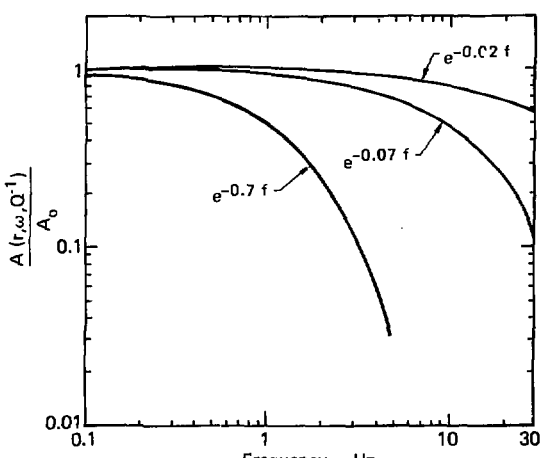

Fig. 7. The attenuation function in Eq. (48) vs frequency. The two curves show the effect of an increase of a factor of 10 in the ratio (r/Q).

A third assumption is that the wave propagates elastically in a one-dimensional, spherical-divergent flow. This, of course, eliminates from consideration applications where free surfaces, other interfaces, or asymmetry in the source contribute significantly to the data that are to be compared.

A fourth assumption, and perhaps the most difficult to justify, is that a forcing function can be chosen to represent the actual pressure-time (or stress-time) history that occurs at the elastic radius. In most of the applications that will be considered, particle-velocity or stress-time histories are available. However, some of these data are limited, giving at most the first positive and first negative phase of the waves. Thus, some error is introduced in the extrapolation of the pressure pulse. The effect of depth of burial has not been introduced in this treatment but has been considered in the work by Murphy (see, for example, Ref. 9).

APPLICATIONS

SALMON

The Salmon experiment was a 5.3 ± 0.5-kt nuclear explosion fired in the Tatum salt dome.[14] The particle-velocity-time histories recorded by Perret[13] suggest that the form of the forcing function at the elastic radius can be approximated by either

$$p(t) = 0 \text{ for } t < 0$$
$$p(t) = p_0 e^{-\alpha t} \text{ for } t \geq 0 \tag{36}$$

or

$$p(t) = 0 \text{ for } t < 0$$
$$p(t) = p_0 e^{-\alpha t} + p_0 \text{ for } t \geq 0 \tag{28}$$

From Perret's report the volume in the cavity created by the explosion was estimated to be equivalent to a cavity radius of 21 m. This volume must be accounted for either by the closing of preexisting porosity, by permanent displacement, or by a combination of these two effects. We can use Eq. (28) as our forcing function if we assume that all of the volume goes into incompressible, permanent displacement of the salt surrounding the cavity. The fact is that the porosity at the Salmon site may be zero, and Perret's measurements of permanent displacement, which show a great deal of scatter, do not invalidate this assumption. Thus we can calculate the permanent displacement using Eq. (32)

$$\xi_R(r) \simeq \frac{3087}{r^2} \text{ m}, \tag{32}$$

or $|\phi(\infty)| = 3087 \text{ m}^3$.* From Perret's experimental measurements (Perret, 1966) and from sonic logs of the Tatum salt, we know

$$\alpha^{-1} = 0.02 \text{ s}$$
$$\mu = 1.5 \times 10^5 \text{ bar}$$
$$\beta = 3/4$$
$$c = 4550 \text{ m/s}.$$

In a reasonable range of the parameters for the Salmon event, the maximum value of the displacement potential $|\hat{\gamma}^*(\eta)|$ [Eq. (30)] occurs at a frequency corresponding to $\eta \simeq 1$ (i.e., when $\omega \simeq \omega_0$). Perret states that the frequency for peak amplitude occurred at approximately 2.5 Hz. Therefore, the elastic radius a_0 is at approximately 290 m

*This calculated value of $|\phi(\infty)|$ is also consistent with Perret's measurements of $|\phi(\infty)|$.

$$a_0 = \frac{c}{\omega_0} = \frac{4550\ \text{m}}{2\pi(2.5)} = 290\ \text{m}.$$

Based upon Perret's measurement, the peak stress, $p_s + p_0$, at 290 m is equal to 395 bar. Now, using the above results and Eq. (34), we can calculate p_0, the steady-state stress:

$$p_0 = \frac{4|\sigma(\infty)|\mu}{a_0^3} = \frac{4(3087)(1.5 \times 10^1)}{(290)^3} = 76\ \text{bar}.$$

Rewriting Eq. (30), we get

$$2\pi|\tilde{\gamma}(\omega)| = \frac{p_0 a_0^3}{4\mu}\left[\frac{\eta^2\left(\frac{p_s}{p_0}\right)^2\left(1 + 2\frac{p_0}{p_s}\right)}{\eta^2 + \left(\frac{\alpha}{\omega_0}\right)^2} + 1\right]^{1/2}\left[\frac{1}{1 - (2\beta - 1)\eta^2 + \beta^2\eta^4}\right]^{1/2}, \qquad (49)$$

or upon substituting the known values,

$$2\pi|\tilde{\gamma}(\omega)| = 3087\ \text{m}^3\left[\frac{0.4108\ f^2}{0.0158\ f^2 + 1}\right]^{1/2}\left[\frac{1}{1 - 0.08\ f^2 + 0.0144\ f^4}\right]^{1/2}. \qquad (50)$$

In Fig. 8, Eq. (50) is plotted and compared with measurements reported by Springer et al.[15] The calculated curve represents a "best guess" calculation of Salmon based upon the data reported by Perret.

In Fig. 9, calculations using two other values of the elastic radius are shown and compared with the observed data. It is apparent in this comparison that the calculation with the elastic radius at 240 m ($f_{max} = 3$ Hz) agrees as well, if not better, with the experimental results as the calculation using 290 m. This is not surprising since the data presented by Springer et al. show a peak in the velocity potential at about 3 Hz. Even better agreement with experiment is obtained when an attempt to compensate for the effects of internal friction is made. In this adjustment, shown by the arrows in Fig. 9, it was assumed that Q was 550 and that the range was 16 km (i.e., the range to one of the observation stations used in getting the experimental data).

In Fig. 10, the calculation based upon Eq. (50) is compared with a calculation using the forcing function described by Eq. (36). Using Eq. (36) is equivalent to assuming that sufficient porosity exists in the material so that p_0 approaches zero and there is negligible permanent displacement at and beyond the elastic radius. As Fig. 10 shows, the removal of permanent displacement considerably reduces the amount of low frequency content in the far-field spectrum.

These comparisons show that the function $p(t) = p_s e^{-\alpha t} + p_0$ does an excellent job of representing the regional seismic data from the Salmon event when the elastic radius is chosen in the 240-290-m range and adjustments are made to the calculation to compensate for the effect of internal friction.

STERLING

The Sterling experiment was a 0.38-kt nuclear explosion fired in the cavity produced by the Salmon nuclear event. The Salmon cavity, with a radius of 17.4 ± 0.6 m, is nearly spherical and partially filled with melt and measurements of the volume of the cavity, given an equivalent sphere radius of 16.7 ± 0.6 m. Various criteria are available to test whether total decoupling of the Sterling explosion is achieved in this volume. According to the Latter decoupling criteria, 0.21-0.42 kt are decoupled depending on whether the initial spike in pressure produced by the explosion and hitting the cavity wall can be ignored.[5] The Sterling explosion is in the upper range of these criteria; therefore, we will measure the effect of a pressure spike by comparing ideal decoupling [Eq. (25)] with a calculation based on Eq. (30).

For an ideal decoupled shot, the forcing function is $p(t) = p_0$, where p_0 for the Sterling conditions is given by

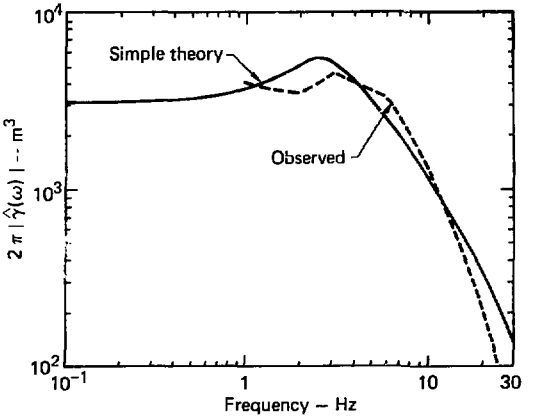

Fig. 8. Comparison of a calculation using Eq. (50) with the observed reduced velocity potentials for Salmon.

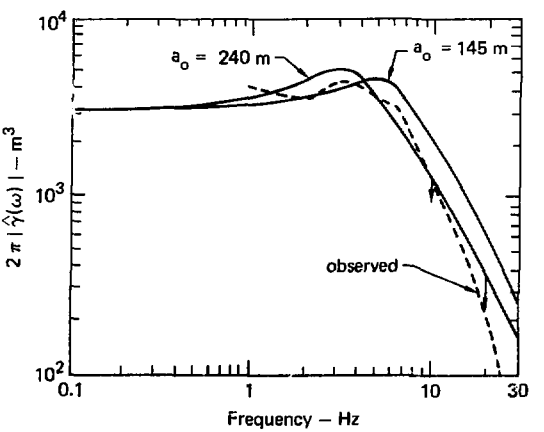

Fig. 9. Comparison of calculations using Eq. (50) with the observed reduced velocity potentials for Salmon.

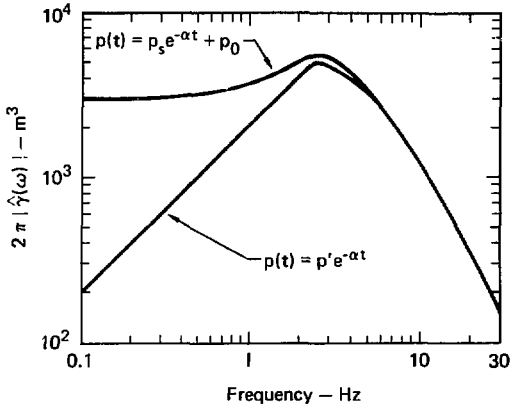

Fig. 10. A comparison of a calculation for Salmon using Eq. (50) with one using Eq. (36) and assuming p′ = 395 bar.

$$p_0 = \frac{\Gamma 3W}{4\pi a_0^3} = \frac{3(0.2)(0.38)(4.18 \times 10^{19}\text{erg})}{4\pi(16.7\text{ m})^3\left(\frac{10^{12}\text{ erg}}{\text{m}^3\text{ bar}}\right)} = 163\text{ bar}$$

where the value of 0.2 for Γ is a value appropriate for air.[5] Rewriting Eq. (25), we have

$$2\pi|\tilde{\gamma}(\omega)| = \frac{p_0 a_0^3}{4\mu}\left[\frac{1}{1 - (2\beta - 1)\eta^2 + \beta^2\eta^4}\right]^{1/2} . \tag{51}$$

For Sterling, the salt out to a radius of approximately 83 m had been altered by the Salmon explosion. As a result, measurements indicated that c = 3820 m/s, $\mu = 1.0 \times 10^5$ bar, and $\beta = 3/4$.* Substitution of these values into Eq. (51) gives

$$2\pi|\tilde{\gamma}(\omega)| = 2.15\text{ m}^3\left(\frac{1}{1 - 4.09 \times 10^{-4}f^2 + 3.77 \times 10^{-7}f^4}\right)^{1/2} . \tag{52}$$

Equation (52) is plotted in Fig. 11 along with measurements reported by Springer et al.[15]

A measure of the effect of the first pressure spike hitting the wall in the Sterling experiment is given by Eq. (30)

$$2\pi|\tilde{\gamma}(\omega)| = \frac{p_0 a_0^3}{4\mu}\left[\frac{\eta^2\left(1 + 2\frac{p_0}{p_s}\right)\left(\frac{p_s}{p_0}\right)^2}{\left(\frac{\alpha}{\omega_0}\right)^2 + \eta^2} + 1\right]^{1/2}\left[\frac{1}{1 - (2\beta - 1)\eta^2 + \beta^2\eta^4}\right]^{1/2} .$$

*Assumption of these parameters will give a maximum value for the reduced-velocity potential assuming elastic behavior.

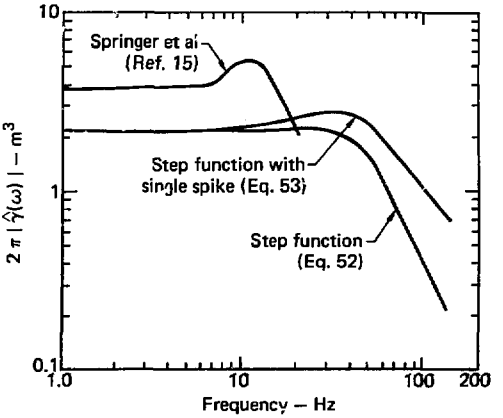

Fig. 11. A comparison of theory with results deduced from the Sterling experiment.

Using values of $\alpha = 5000\ s^{-1}$ and $p_c = 3200$ bar, which seem appropriate based upon the Cowboy experiments[6] and the calculations made by Patterson,[7] we get the following relationship:

$$2\pi|\hat{\gamma}(\omega)| = 2.15\ m^3 \left(\frac{1.676 \times 10^4\ f^2}{2.5 \times 10^7 + 39.48\ f^2} + 1\right)^{1/2} \cdot \left(\frac{1}{1 - 4.09 \times 10^{-4} f^2 + 3.77 \times 10^{-7} f^4}\right)^{1/2} \quad (53)$$

Equation (53) is also plotted in Fig. 11.

The differences that exist between the theoretical calculation and the experimental observation in the Sterling experiment are difficult to explain conclusively. However, the observation of a corner frequency at approximately 10 Hz implies a cavity with a radius of at least 40 m, assuming full decoupling

$$\eta_{max} = \frac{\omega_{max}}{\omega_0} = \frac{2}{3} \ ;$$

therefore

$$a_0 \simeq \left(\frac{2}{3}\right)\frac{c}{2\pi f_0} \geq \left(\frac{2}{3}\right)\frac{3820}{2\pi(10)} \simeq 40\ m \ .$$

This is inconsistent with the actual cavity radius of 17.4 m and suggests that Sterling was not fully decoupled. Therefore, assuming Sterling was not fully decoupled, it is not surprising to see a difference of a factor of ~ 2 in the observed and predicted reduced velocity potentials.

DECOUPLING—STERLING COMPARED TO SALMON

A measure of the effectiveness of a cavity to decouple an explosion is given by a direct comparison as a function of frequency of the amplitudes of a tamped shot to those of a decoupled shot. This comparison is made

for Salmon and Sterling in Fig. 12 using both calculations and measurements. However, comparisons to determine decoupling are more useful if they are made with both shots at the same energy yield. To make this latter comparison, we shall define the decoupling $D(f)$, as the ratio of the reduced velocity potentials determined at the same energy yield, W, and at the same frequency

$$D(f) = \frac{|\tilde{\gamma}(f)|_{\text{tamped}}}{|\tilde{\gamma}(f)|_{\text{decoupled}}} \quad , \tag{54}$$

and use the following cube-root scaling equation to scale from one yield W_2 to another yield W_1

$$\tilde{\gamma}_1(f_1) = \frac{W_1}{W_2}\,\tilde{\gamma}_2\left[\left(\frac{W_2}{W_1}\right)^{1/3} f_2\right]$$

Using Eq. (55) we have assumed time and distance scale as $W^{1/3}$ and that gravity does not influence our results.

In Fig. 13 the calculated reduced velocity potentials are plotted for Salmon and for Sterling, scaled to the Salmon yield using Eq. (55). The ratio of these two curves is shown in Fig. 14 along with decoupling results from the experimental data reported by Springer et al.[15] The differences are a direct result of the differences that occur between experimental and calculated velocity potentials for Sterling.

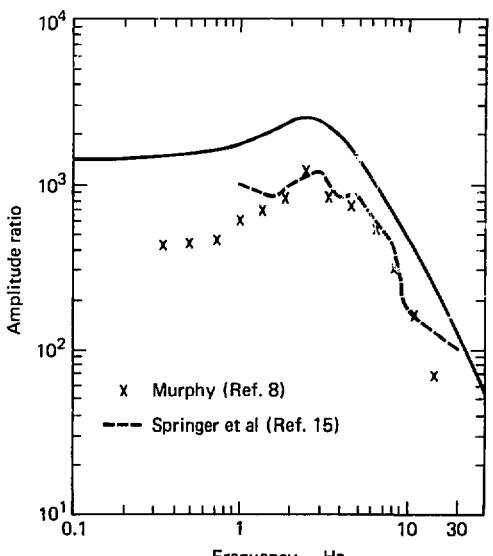

Fig. 12. A comparison of calculated and measured amplitude ratios for Salmon and Sterling.

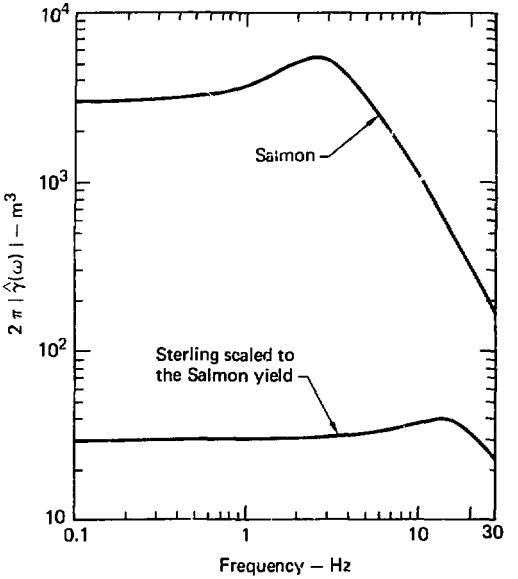

Fig. 13. A comparison of the Salmon and Sterling experiments using the simple theory with Sterling scaled to the Salmon yield.

DISCRIMINATION BETWEEN TAMPED AND DECOUPLED EXPLOSIONS

The calculated reduced velocity potentials displayed in Fig. 13 suggest the possibility of comparing measurements near the corner frequency with those at significantly higher frequencies as a means of discriminating between tamped and decoupled explosions. In Fig. 13, measurements at 2.5 Hz and 20 Hz would give an amplitude ratio of ~ 20 for an explosion that was tamped, but only a ratio of approximately one for an explosion that was decoupled. Therefore, it seems reasonable that regional sites (to minimize the high-frequency filtering of the earth) equipped with high-frequency passbands to monitor frequencies of the spectrum in the range of 1–20 Hz or greater, could serve to discriminate between tamped and decoupled explosions.

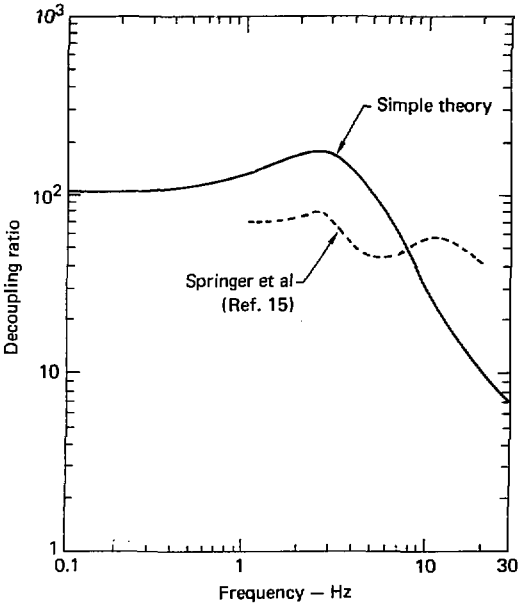

Fig. 14. A comparison of the Salmon and Sterling decoupling ratio as a function of frequency.

SUMMARY

1. In an ideal decoupling experiment, granite could be as much as three times more effective as a decoupling medium than sodium chloride.
2. The series of spikes superimposed on a step-pressure pulse in an explosive decoupling shot causes a large perturbation on the observed spectrum at the higher frequencies (i.e., beyond the corner frequency).
3. The rise times of pressure pulses seen in consolidated rocks (those with little dry porosity) are typically of the order of, or less than, one-tenth the width of the pulse that propagates in the elastic regime. In these cases the effect on the spectrum is small, except for frequencies beyond four times the corner frequency. However, for pressure pulses characteristic of dry porous rocks or frozen soils (i.e., slow rise times), the spectrum is significantly altered predominantly at the higher frequencies.
4. The regional seismic data from Salmon is well represented by the theory if a forcing function of form $p(t) = p_1 e^{-\alpha t} + p_0$ is used and the elastic radius, a_0, chosen is between 240–290 m.
5. Comparison of calculations and experimental observations from the Sterling event suggest that Sterling was not fully decoupled. The experimentally observed lower corner frequency (10 Hz vs 35 Hz) and higher reduced velocity potential (by a factor of about two) are both consistent with partial decoupling.
6. Theoretical calculations suggest that regional sites equipped with high-frequency passbands to monitor frequencies of the spectrum in the range of 1–20 Hz or greater, could serve to discriminate between tamped and decoupled explosions.